The Astrophysical Journal, 769:43 (13pp), 2013 May 20 doi:10.1088/0004-637X/769/1/43

TRACKING CORONAL FEATURES FROM THE LOW CORONA TO EARTH: A QUANTITATIVE ANALYSIS OF THE 2008 DECEMBER 12 CORONAL MASS EJECTION

C. E. DeForest[1], T. A. Howard[1], and D. J. McComas[2,3]
[1] Southwest Research Institute, 1050 Walnut Street, Suite 300, Boulder, CO 80302, USA; deforest@boulder.swri.edu
[2] Southwest Research Institute, 6220 Culebra Rd., San Antonio, TX 78249, USA
[3] Department of Physics and Astronomy, UTSA, San Antonio, TX 78249, USA
Received 2012 December 11; accepted 2013 March 18; published 2013 May 3

ABSTRACT

We have tracked a slow magnetic cloud associated coronal mass ejection (CME) continuously from its origin as a flux rope structure in the low solar corona over a four-day passage to impact with spacecraft located near Earth. Combining measurements from the *STEREO*, *ACE*, and *Wind* space missions, we are able to follow major elements with enough specificity to relate pre-CME coronal structure in the low corona to the corresponding elements seen in the near-Earth in situ data. Combining extreme ultraviolet imaging, quantitative Thomson scattering data throughout the flight of the CME, and "ground-truth" in situ measurements, we: (1) identify the plasma observed by *ACE* and *Wind* with specific features in the solar corona (a segment of a long flux rope); (2) determine the onset mechanism of the CME (destabilization of a filament channel following flare reconnection, coupled with the mass draining instability) and demonstrate that it is consistent with the in situ measurements; (3) identify the origin of different layers of the sheath material around the central magnetic cloud (closed field lifted from the base of the corona, closed field entrained during passage through the corona, and solar wind entrained by the front of the CME); (4) measure mass accretion of the system via snowplow effects in the solar wind as the CME crossed the solar system; and (5) quantify the kinetic energy budget of the system in interplanetary space, and determine that it is consistent with no long-term driving force on the CME.

Key words: Earth – interplanetary medium – solar–terrestrial relations – solar wind – Sun: coronal mass ejections (CMEs) – Sun: corona – Sun: filaments, prominences – Sun: heliosphere

Online-only material: animations, color figures

1. INTRODUCTION

Coronal mass ejections (CMEs) are major sources of the open solar magnetic field, transfer mass and energy from the corona to the heliosphere, and are important causes of space weather. Yet tracing them from the Sun outward through the heliosphere has proven difficult. This fact is reflected in the terminology used to describe the systems. The terms "CME" and "ICME" have been used to describe similar systems viewed near the Sun by coronagraphs (e.g., Gopalswamy et al. 2009) and in situ in interplanetary space by plasma instruments (e.g., Dryer et al. 1992; Cane & Richardson 2003; Zurbuchen & Richardson 2006). The phrase "CME" is used differently by the remote-sensing and in situ communities, to mean either the entire dense (and therefore observable) system of ejecta visible in a coronagraph (e.g., Howard et al. 1985; Hundhausen 1993; Gopalswamy et al. 2009) or that subset which retains connectivity to the corona when viewed in situ (e.g., Gosling et al. 1987). Now that heliospheric imagers extend the coronagraph field of view well beyond the actual corona, these two terms, with their slightly different meanings, collide. In this work, we use the term "CME" to refer to the complete remotely observable propagating system, including the flux rope, surrounding sheath material, and any other solar wind or coronal material entrained enroute. We use "ICME" to refer instead to the more restricted physical system that excludes entrained solar wind, as can be distinguished by in situ measurements of domain boundaries and solar connectivity.

The onset processes for CMEs, including triggering and launch, remain uncertain despite decades of observation and modeling. This results, in large part, from the difficulty of associating pre-CME and early CME structures seen remotely in the solar corona with particular magnetic and density structures detected in situ. Most prominence-associated CMEs appear to have a three-part structure, with a bright front, a dark visible cavity that is considered to be a flux rope seen end-on, and a bright, cool core associated with prominence material (Illing & Hundhausen 1986; Forbes 2000; Hudson et al. 2006). The central flux rope core is often identified with magnetic clouds (Burlaga 1988) observed in situ and, although rarefied, is not generally fully evacuated in the solar wind nor the corona (Fuller et al. 2008). Pre-eruption, the prominence and CME material are thought to be held down by some combination of: an overlying magnetic flux domain that restrains them via the tension force until released via reconnection or ideal instability (Antiochos et al. 1999; Forbes 2000; Fan & Gibson 2007; Rachmeler et al. 2009); and the mass of the prominence itself, which can destabilize the system by fully or partially draining if its containing magnetic dip vanishes (Klimchuk & Sturrock 1992; Fong et al. 2002; Gibson & Fan 2006; Zhou et al. 2006).

The erupting structures comprising a flux rope CME then consist of the central erupting flux rope core and perhaps an associated prominence, with an overlying sheath of closed field lines bound to the Sun. The sheath may contain field lines from the "strapping field" that formerly restrained the CME system, and also any other closed field lines that were present higher above the erupting structure. This view imposes another problem: stretching the surrounding field far from the corona can increase the free energy of the magnetic field, which in turn can cause the post-eruption total magnetic energy to be greater than that of the pre-eruptive state. This paradox, which applies to force-free fields and low-β plasmas (as in the lower corona), has become known as the Aly–Sturrock energy limit (Aly 1984, 1991; Sturrock 1991). A purely magnetically driven

CME would not be expected to spontaneously erupt under such conditions as it would not be energetically favorable for it to do so. That result is of concern because the magnetic field is the only coronal energy reservoir with sufficient energy to launch a CME (e.g., Low 1996).

Several mechanisms have been proposed to address the issue of magnetic driving and release. Although real events include multiple energy sources, they may be classified by main instability: de-stabilization via mass draining (mass draining: Klimchuk & Sturrock 1992; Fong et al. 2002; Gibson & Fan 2006; Zhou et al. 2006); emergence of sub-solar magnetic flux into a stable field (flux injection: Chen 1989, 1996); driven reconnection caused by kinking when a flux system becomes excessively twisted and begins to writhe (kink instability: Török & Kliem 2003, 2005; Fan & Gibson 2003, 2004); runaway magnetic reconnection either below the CME core field (tether cutting: Moore et al. 1987; Moore & Roumeliotis 1992) or between the core and the original strapping field (breakout: Antiochos et al. 1999; Lynch et al. 2008); and ideal herniation of the core field through a strapping field (herniation: Rachmeler et al. 2009).

In the last three models, the surrounding field is disposed of by either being incorporated into the main flux system (tether cutting), being removed by overhead reconnection (breakout), or being swept aside by ideal instabilities (herniation). All three of these models require that little of the surrounding strapping field be carried into the heliosphere by the CME. On the other hand, mass draining and flux injection both rely on destabilization irrespective of the strapping field. In the kink instability model, strapping field may or may not play a large role in initial restraint of the system. Each of these models should leave a distinctive topological signature in the erupting system.

Magnetic connectivity in the solar wind in general is identified in situ by the behavior of field-guided energetic particles. Field-guided suprathermal energetic electrons stream outward from the Sun, spiraling around magnetic field lines, and indicate the direction along the field of magnetic connectivity to the Sun. Counterstreaming suprathermal electron flows are commonly observed within CMEs in the solar wind and are interpreted as a sign of newly opened magnetic flux with dual connectivity to the Sun (e.g., Gosling 1990, 1993, and references therein). Yet these analyses have been hampered by lack of direct association between structures observed in situ in interplanetary space and their counterparts in the lower corona in the pre-eruptive system, because the counterstreaming electrons contain no information about which locations on the disk are the footpoints of the connected field lines.

With recent advances in heliospheric imaging, several authors have used qualitative imaging to track CMEs through the heliosphere from the Sun to impact with an in situ probe or the Earth's magnetosphere. Howard & DeForest (2012a) followed the 2008 December 12 CME from Sun to Earth using the starfield-removed imagery from the integrated SECCHI suite on board *Stereo-A*; Wood et al. (2012) tracked the 2009 June 22 CME using the Naval Research Laboratory (NRL) background model and J-map analysis; Savani et al. (2012) used similar non-imaging analysis to track the evolving shape of several CMEs; and Lugaz (2012) and Möstl et al. (2012) have each recently analyzed a single CME or cluster of CMEs with a combination of morphological and J-map remote sensing analysis and in situ data.

In this paper, we report on the use of quantitative, starfield-subtracted photometric imagery to make the association of particular image features observed remotely in the solar corona in a pre-CME eruptive structure (the CME of 2008 December 12), with a magnetic field and density structures observed in situ when the CME impacted a near-Earth probe (*ACE*). We identify particular pieces of the CME's anatomy in situ with their associated coronal features in the pre-eruptive structure, and track the mass and kinetic energy of the CME as it crosses the solar system. Informed both by the event's structure detected in situ and by its inferred relationship to the coronal CME structure as observed during early flight through the low corona, we construct a clear, data-supported narrative detailing the process of eruption and the evolution that occurred as the CME traversed the corona and inner heliosphere.

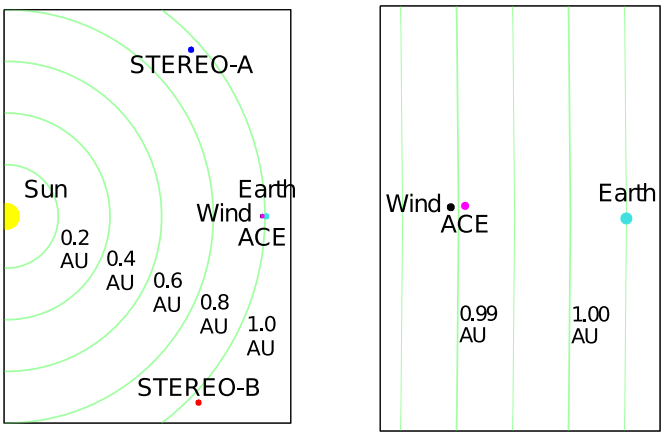

Figure 1. Solar system and observer geometry for the 2008 December 12 CME, as seen looking "down" on the ecliptic from the north ecliptic pole. Left: *STEREO-A* and *STEREO-B* were 42° ahead and behind the Earth, respectively. Right: *Wind* was slightly upstream from *ACE* near the L1 point; Earth was at 1.005 AU.

(A color version of this figure is available in the online journal.)

2. DATA

We have merged in situ and quantitative remote sensing data from the CME that was launched from the Sun on 2008 December 12. Previous reports on this CME appear in Davis et al. (2009), Liu et al. (2010), Lugaz (2010), Byrne et al. (2010), DeForest et al. (2011), and Howard & DeForest (2012a). The remote sensing data are from the SECCHI imaging suite on board *STEREO-A*, and the in situ data are from *ACE* (Smith et al. 1998; McComas et al. 1998) and *Wind* (Lepping et al. 1995; Ogilvie et al. 1995). The geometry of the four spacecraft and Earth is shown in Figure 1.

2.1. SECCHI Integrated Remote Sensing Data

In 2008 December, *STEREO-A* was 42° ahead of the Earth in its orbit and was well positioned to view the geoeffective CME that left the Sun on 2008 December 12. The SECCHI imaging suite comprises the EUV Imager (EUVI), the COR1 and COR2 coronagraphs, and the HI-1 and HI-2 heliospheric imagers. We have previously described the reduction of heliospheric imaging data from SECCHI (DeForest et al. 2011; Howard & DeForest 2012a) and how to combine the fields of view to track individual features to beyond 1 AU (DeForest et al. 2012). We used the NRL-supplied SECCHI_PREP software to calibrate the individual instruments' measured intensities. We merged the SECCHI fields of view into a single image plane in logarithmic azimuthal coordinates as in Howard & DeForest (2012a). Figure 2 shows important features seen by SECCHI

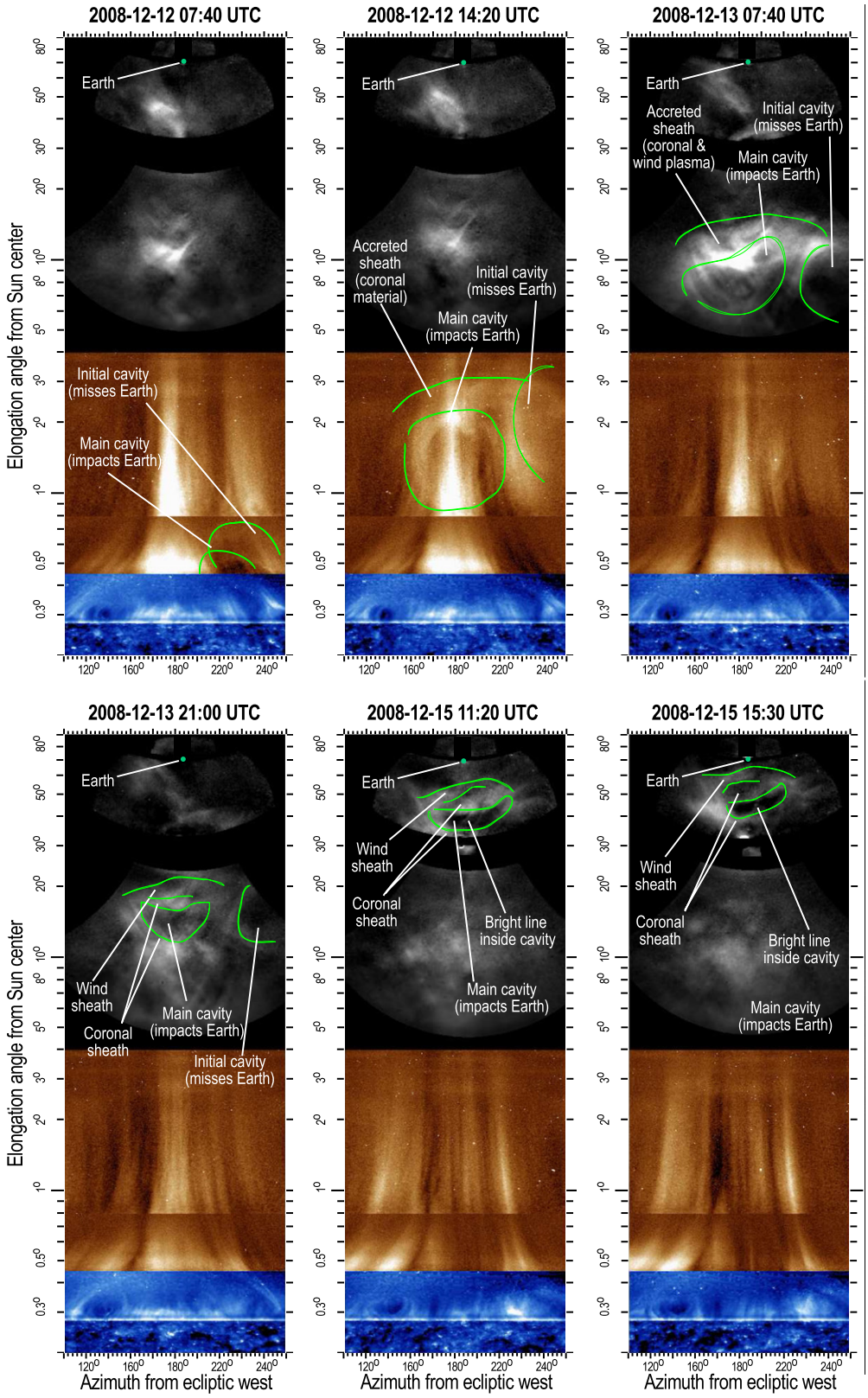

Figure 2. Morphology and evolution of the 2008 December Earth-directed CME were imaged by the integrated SECCHI suite on board *Stereo-A*. Six panels show evolution from formation (upper left) through just before impact (lower right). The Earth-directed CME was triggered by a smaller, more northerly CME that erupted just before and was not Earth-directed. The main cavity in these images is the magnetic cloud in Section 2.2.

throughout the evolution of the CME. The top left panel shows early coronagraph observations of the CME, showing it as a dark cavity eruption at about 40° azimuth that triggers a larger, secondary "main" cavity eruption. This secondary cavity erupts into the streamer belt, propagates across the solar system, and impacts Earth's magnetosphere.

The overlain boundaries in Figure 2 are drawn by direct visual inspection. They approximate clearly visible edges in the data.

The lone exception is the boundary between the "wind sheath" and "coronal sheath" in the bottom three images of Figure 2. That boundary is speculative and is based on the inference (elaborated in the following sections) that the overall structure mass increases via snowplow pickup of the surrounding solar wind as it passes through the inner heliosphere. The morphology of this CME in the outer corona and heliosphere has already been described in detail by Howard & DeForest (2012a).

The main cavity forms into a "classic three-part" CME structure with a leading dense (bright) sheath wall, a main dark cavity, and trailing bright material (Byrne et al. 2010) that may be associated with the pre-eruption filament. The cavity gradually distorts as it propagates. It also accretes material in the leading sheath, which grows thicker during propagation through the corona and continues to grow during passage across the solar system, ultimately becoming lenticular in shape and filling the space between a visually convex leading edge of the bright CME structure and visually concave leading edge of the cavity/void. Howard & DeForest (2012a) provide measurements of this distortion, together with details of the geometry and speed of propagation, and the evolving morphology of the structure.

The CME is first seen in the EUVI and COR1 fields of view at 2008 December 12 07:00 UT; the full initially-circular flux rope was visible to COR1 and COR2 from 2008 December 12 12:00–18:00 UT; and was fully visible in HI-1 and HI-2 from 2008 December 13 03:00 UT to the exit of the trailing edge from the HI-2 field of view early on 2008 December 18.

The cavity is seen to be a magnetic cloud (Burlaga 1988) on arrival at the *Wind* and *ACE* spacecraft during the UT morning of 2008 December 17 (Howard & DeForest 2012a). By the time of impact, this flux rope was distorted to have a concave banana-shaped meridional cross section as seen at the lower right of Figure 2. The impact timing with *ACE* and *Wind* agrees within better than 30 minutes with arrival time estimates for the leading edge and the identified magnetic cloud/cavity edge. In situ results are further elaborated in Section 2.2.

The leading dense (bright) portion of the CME, ahead of the central cavity, grew quickly in size through the corona and continued to grow rapidly thicker as the CME propagated across the solar system. In addition to changing in shape, the CME accreted mass as it propagated.

We measured the CME's mass evolution via quantitative Thomson imaging. We manually marked the region around the propagating CME structure in each frame in our data set that contained a complete image of the CME. We derived the mass with the techniques described by DeForest et al. (2012) and Howard & DeForest (2012b): we treated the CME as a collection of electrons concentrated on the plane defined by the out-of-sky-plane angle ξ defined by Howard & DeForest (2012b) and the viewing angle as determined from the pixel geometry. Given the *STEREO-A* position and the fact that the CME impacted the Earth, the sky angle ξ of the CME centerline is approximately 45°. This places the CME on the Thomson plateau, and simplifies mass calculation by reducing sensitivity to the actual value of ξ (Howard & DeForest 2012b).

Figure 3 shows the inferred mass profile through three instrument fields of view. The mass approximately doubles from the top of the corona (in the COR2 field of view) to 0.7 AU (in the HI-2 field of view). The mass varies from 1 Pg (Pg = Petagram, 10^{15} g) at the top of the corona to just over 2 Pg just before arrival at *ACE*. Acknowledging the gaps between the COR-2 field of view, the processed HI-1 field of view, and the

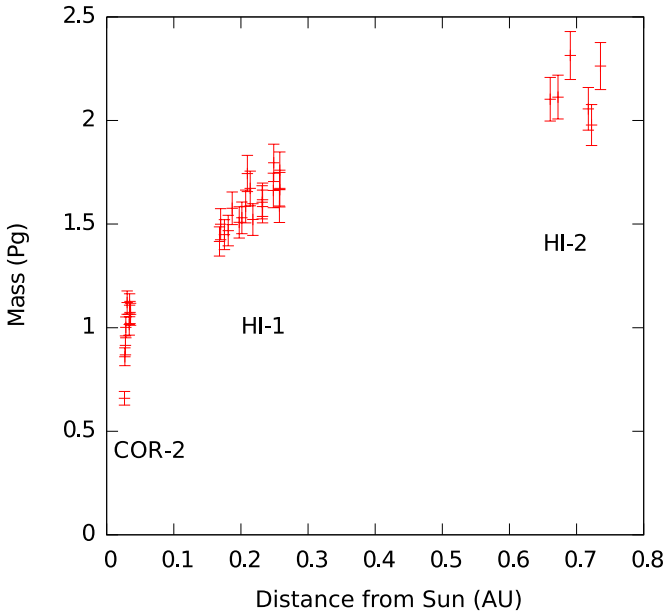

Figure 3. Mass of the 2008 December 12 CME vs. projected center-of-brightness position along the Earth-Sun line, as inferred from *STEREO-A* Thomson scattering photometry. We consider the CME to include compressed material encountered enroute (see text). The large gaps in coverage are due to our rejection of all image frames where even a portion of the CME fell between instrumental fields of view.

(A color version of this figure is available in the online journal.)

processed HI-2 field of view, we omitted any points in which any part of the CME appeared to be in the gap, leading to the clustered points in Figure 3. The error bars are determined by adding, in quadrature, two calculated noise terms: uncertainty in average radiance due to the noise level in the images, which was determined a posteriori from high spatial frequencies in the image sequences themselves; and uncertainty in intensity due to feature boundary location error, which was estimated by recalculating the feature estimated mass after dilating or contracting the feature by two instrument pixels.

CME mass growth has been observed with coronagraphic imaging (e.g., MacQueen et al. 1980; Brueckner et al. 1995), and has been noted by comparison between measured coronal mass and inferred mass from densities measured in situ. Our tracked measurements are to our knowledge the first fully empirical (model-independent) Sun-to-Earth measurement of CME growth and total mass increase from the low corona across the solar system.

2.2. In situ Data from ACE and Wind

The CME passed over both *ACE* and *Wind* in a 42 hr period. The arrival time of the edges of the separate magnetic structural regimes coincided with visual arrival time of the features based on the HI-2 analysis, as described by DeForest et al. (2011) and Howard & DeForest (2012a). The two spacecraft were separated by roughly 190 Mm in the radial direction, corresponding to a 9.5 minute delay at the measured wind speed of 340 km s^{-1}, and features measured by both spacecraft were observed with a delay of between 8 and 13 minutes. We have taken magnetic and suprathermal electron pitch angle distribution data from *ACE*/MAG (Smith et al. 1998) and *ACE*/SWEPAM (McComas et al. 1998) instruments. The *ACE* density data were unreliable during this interval, so we instead used the *Wind*/SWE instrument (Ogilvie et al. 1995) for density and speed. The two

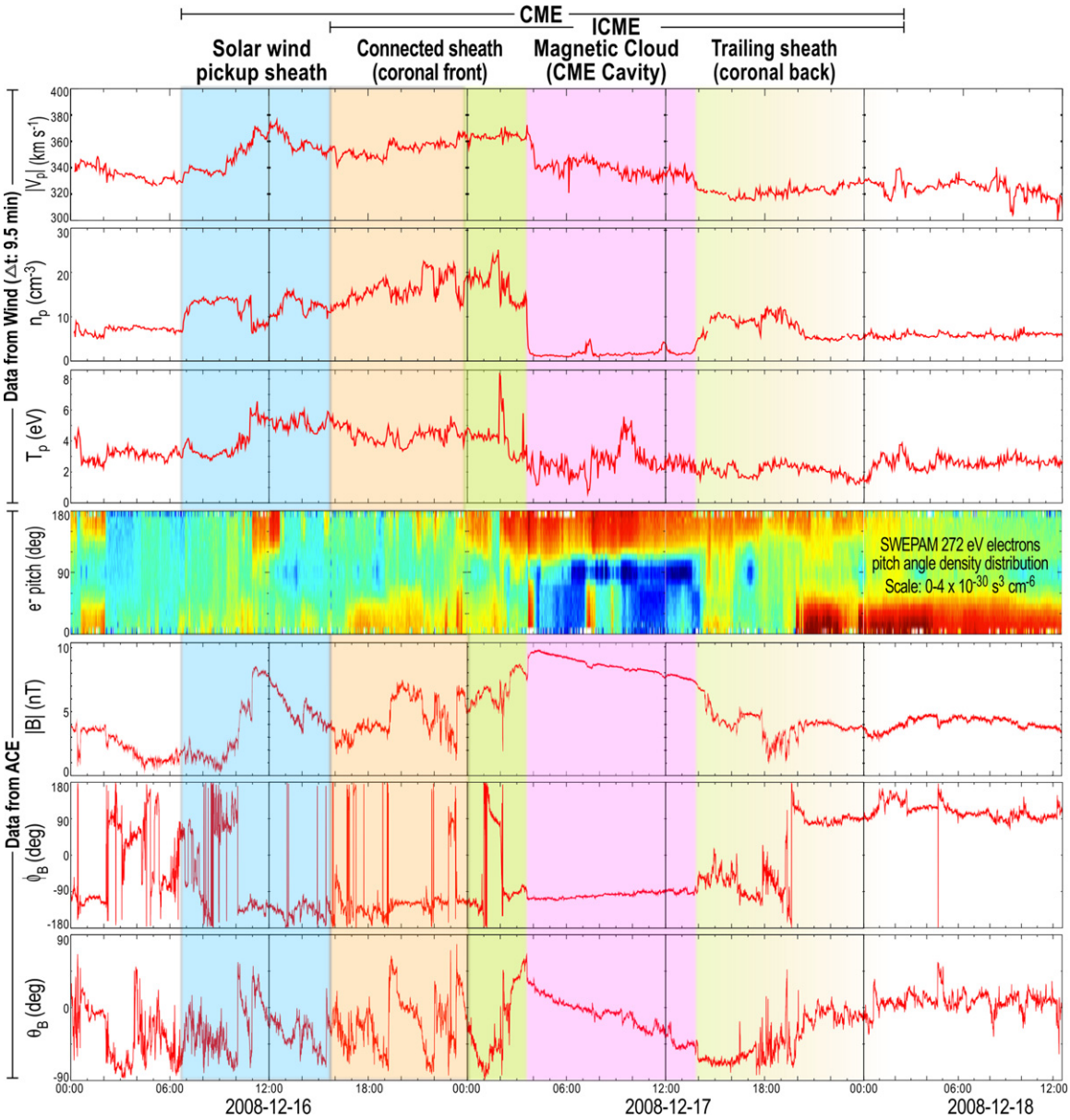

Figure 4. Key quantities measured in situ by the *ACE* and *Wind* spacecraft as they encountered the CME of 2008 December 12, four days after onset. From top to bottom: bulk proton wind speed, density, and temperature from *Wind*/SWE; pitch-angle distribution of suprathermal electrons in the 272 eV channel of *ACE*/SWEPAM; magnetic strength and angle from *ACE*/MAG. The *Wind* data are delayed 9.5 minutes to account for travel time between the two spacecraft. See text for interpretation and discriminants of the marked regions.

spacecraft were close to each other and nearly in syzygy with the Sun (Figure 1), enabling hybrid analysis of CME-scale features in the near-Earth solar wind.

First contact of the leading sheath regime with *ACE* was just before 2008 December 16 07:00 UT, almost exactly four days after the launch of the flux rope (Section 2.1). A corresponding solar wind density enhancement lasted until the encounter with the magnetic cloud beginning at 2008 December 17 03:30 UT. Examination of the pitch angle distribution plots of supra-thermal electrons as measured by *ACE*/SWEPAM divides the density-enhanced period into an initial time of little counterstreaming electron activity from 2008 December 16 07:00–16:30 UT, and a following time in which counterstreaming is readily visible in the pitch angle distributions of 272 eV and other electrons. (We have plotted only the 272 eV distribution for simplicity, but counterstreaming is visible throughout the energy range from 100 eV to 700 eV.) The magnetic cloud crossed from 2008 December 16 03:30 UT to 2008 December 17 02:00 UT. The cloud was followed by further dense material with significant counterstreaming in the 272 eV electron distribution. This trailing material was not well separated from the trailing solar wind in density or magnetic field, but showed significant counterstreaming until 2008 December 18 02:00 UT.

We marked the colored regions in Figure 4 based on the in situ data alone. Here we describe each section and the reason for each boundary's placement.

The marked "solar wind pickup sheath" contains primarily singly connected field lines with some small regions of counterstreaming, as is typical of the slow solar wind. Its leading boundary is defined by a comparatively sudden (but not shock associated) enhancement in the wind proton density, with a rise time of 1 hr, from 8 cm^{-3} to 15 cm^{-3}.

The "connected sheath" is determined by a boundary in the suprathermal electron behavior, with a transition from primarily singly connected field lines to primarily doubly connected field lines with asymmetric counterstreaming intensities. The boundary in the center of the connected sheath is defined by a domain boundary with a simultaneous rotation in the magnetic field and a switch in the direction of the dominant strahl of suprathermal electrons.

The "magnetic cloud" closely fits the definition from Burlaga et al. (1981) and Burlaga (1988). The low-density region has a strong magnetic field, gradual field rotation throughout, and low plasma temperature (Davis et al. 2009; Liu et al. 2010). The boundaries are placed at the edges of the low-density region. This magnetic cloud contains a mixture of singly and doubly connected field lines (as seen in other events by Gosling et al. 1995).

The "trailing sheath" is a density-enhanced region that is dominated by doubly connected field lines, fading gradually to the original solar wind density and a primarily singly-connected state. There is no well defined rear boundary edge, so we instead fade the coloration gradually to white near the beginning of 2008 December 18.

The "CME" label marks the entire density-enhanced region that is visible in Thomson-scattered light with the heliospheric imagers. The "ICME" label marks the edges of the ejected coronal material as identified by the counterstreaming flows.

3. RESULTS AND DISCUSSION

In this section, we combine the quantitative data and draw inferences from them. We also discuss and interpret morphological extreme ultraviolet (EUV) imagery of the pre-eruption system and eruption event from *STEREO*/EUVI.

3.1. Morphology and Connectivity

We use counterstreaming electrons, observed in situ by *ACE*/SWEPAM, as an indicator of magnetic connectivity to the Sun (e.g., Gosling et al. 1987, 1992). Because of the lack of consistent counterstreaming in the initial density enhancement (the blue shaded "solar wind pickup sheath" in Figure 4), indicating a field regime that is mostly not doubly connected to the Sun, we identify this dense region as a pressure wave of solar wind material picked up from the ambient solar wind ahead as the CME propagated outward from the Sun. The density in this wind sheath alone was enhanced by a factor of 1.9 compared to the wind prior to the pressure wave. Taking the density prior to the enhancement to be typical, we may estimate that the nine hour dense region represents approximately eight additional hours of solar wind compressed by the piston action of the ICME front during the four day passage from Sun to Earth. This would require a pressure-wave propagation speed of $\approx$32 km s^{-1}, which is comparable to the computed Alfvén speed of $\approx$33 km s^{-1} in the wind just ahead of the boundary.

This picture of the leading singly-connected sheath being due to the snowplow effect is further supported by the inferred mass growth from the Thomson imagery: the material in the wind sheath represents approximately 30%–40% of the in situ observed mass of the entire structure, with the uncertainty dominated by variations in crossing speed and by the identification of the trailing edge with the end of counterstreaming at 2008 December 17 22:00 UT versus the end of the density enhancement at 2008 December 17 20:00 UT. The total CME mass, inferred from Thomson scattering, increases by a factor of 1.6 from the top of the corona to the middle of the HI-2 field (Figure 3), which is consistent with all of the material in the wind sheath (blue region in Figure 4) being picked up enroute. The picture of the wind sheath dominating the front of the CME is also consistent with its morphological lens shape, described by Howard & DeForest (2012a) who attributed the shape to denser wind encountered in the plane of the ecliptic compared to higher latitudes.

Following the wind sheath is the marked "coronal sheath." It appears to consist of multiple closed magnetic structures hoisted from the corona and carried in front of the magnetic flux rope outward into the solar system. We divide this region into two separate subregions. The two regions are divided by a sudden shift in suprathermal electron pitch-angle distribution and by a small local minimum in the magnetic field strength. We take the inner structures (marked green in Figure 4 and referred to in Section 1) to be a field that originated immediately above the flux rope, and the outer structures (marked orange in Figure 4) to be a high closed coronal field accumulated on the front of the system during the early rise phase. This identification of the two zones is also consistent with observed mass growth as the system rose through the corona: the system doubled in mass as it passed from the bottom to the top of the COR-2 field of view.

The magnetic cloud (magenta in Figure 4) preserves the original "main" flux rope seen as a cavity in the corona. While this association has been posited for years (e.g., Klein & Burlaga 1982), this is the first event for which the association can be made directly through continuous tracking: the sheath and void maintain continuity of form all the way from first visibility in the coronagraphs to arrival at 1 AU (Howard & DeForest 2012a). The association is particularly clear because the magnetic cloud is very deeply evacuated in this CME; though visible voids like this one are far from uncommon (Howard & DeForest 2012a). Density contrast is important to visibility because Thomson-scattering images are sensitive only to line-of-sight integrated electron number density and not to the magnetic field directly. Interestingly, the small density spike observed at 2008 December 17 07:00 UT may correspond with the bright line annotated in the upper-right panel of Figure 2 based on position within the void, and corresponds to a strong counterstreaming-electron event in the middle of the cloud. This suggests that with higher imaging resolution, small tracer structures within CME magnetic flux ropes may be readily observable.

The magnetic cloud contains an interesting feature in the suprathermal electron pitch-angle distribution: a strong depletion of suprathermal electrons from 0° to 90° through most of the void. We speculate that this could be caused by linear expansion of the flux rope, which is multiplied by the winding number, together with asymmetry of the spacecraft path relative to the overall geometry.

After passage of the magnetic cloud is a trailing coronal sheath of structured magnetic material (faded "trailing sheath" in Figure 4), which also features some counterstreaming electrons and contains approximately 10%–20% of the mass of the total structure (determined both from in situ measurement and Thomson imagery). The trailing sheath has multiple connectivities including complete dropouts of the counterstreaming electron beams (e.g., at 2008 December 17 18:00 UT), and has no clear boundary with the surrounding solar wind; this is consistent with the ragged appearance of the rear of the structure in Figure 2.

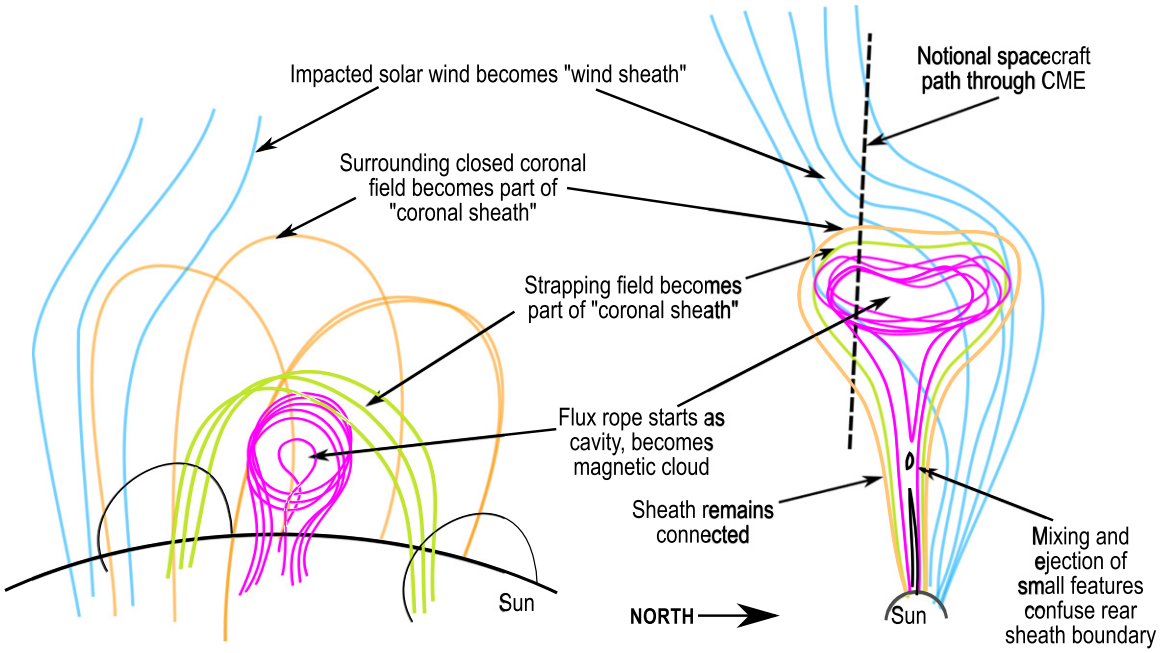

Figure 5. Sketch of inferred magnetic topology and zones for the CME of 2008 December 12 as viewed from *STEREO-A*. A flux rope erupts from the corona toward the Earth, carrying a strapping field with it. The coronal structure is substantially preserved as it crosses the solar system, including plasma entrained in front of the CME flux rope as it passes through the corona. A wind sheath is accumulated on the front of the flux rope as it travels faster than the ambient wind. Reconnections and impact by trailing wind confuse the signature of the trailing edge. The color key matches Figure 4. The strapping and overlying coronal field are distinguished by their slightly different signatures in situ (Figure 4) and by their consistency with the observed mass growth of the overall structure as it rises through the corona and heliosphere (Figures 2 and 3).

Table 1
Conformance Matrix between the 2008 December 12 CME and CME Onset Models

Model/Obs	Cavity Morphology at Bottom of Corona	Cavity Morphology at Top of Corona	Connected Sheath Structure
Observation	Approximate symmetric	Larger leading wall	Larger leading sheath
Breakout (reconnection above)	Larger trailing wall	Symmetric or Larger trailing wall	Symmetric or Larger trailing sheath
Tether cutting (reconnection below)	Larger leading wall	Approximate symmetric walls	Approximate symmetric sheaths
Ideal instability (herniation; kink)	Symmetric front-back	Approximate symmetric walls	Approximate symmetric sheaths
Mass draining	Symmetric front-back	Larger leading wall	Larger leading sheath

3.2. Onset Mechanism

The division of the magnetic structural regimes described in Section 3.1 enables us to produce a global view of their morphology. Figure 5 shows a cartoon diagram of each of the magnetic regimes, from (left) their origins at the Sun to (right) their resulting structure deep in the solar wind. These morphological insights help determine the onset mechanism of the CME. Table 1 is a conformance matrix between the structure we inferred (and sketched in Figure 5) and several leading models of CME onset and early propagation (discussed briefly in Section 1). We have divided the models describing CME onset into four broad categories: onsets that require reconnection above the CME to eliminate confining fields; those that require reconnection below the CME to reduce restraint by the tension force; ideal MHD instabilities that sweep overlying fields aside; and mass draining instabilities that allow the system to entrain an overlying containment field and erupt with it. Two classes of instability—ideal instability and mass draining—are consistent with the behavior throughout the observed range. Mass draining is the most consistent with the observed behavior of the Earth-directed CME, because draining alone does not rely on sweeping away a strapping field of any kind, supporting the observed early front/back symmetry and ultimate asymmetric connected sheath structure.

3.3. Kinetic Energy and Driving

We considered the kinetic energy of the entire CME event at different stages of its evolution, as inferred from both remote sensing and in situ measurement. We sought to ascertain whether a long-term driver continues to push the CME, as suggested by Howard et al. (2007). Mass and kinetic energy inference followed the techniques followed by DeForest et al. (2012) for a flux disconnection event.

For the bulk speed of the event we rely on a combination of the in situ measurements in Figure 4, previously published remotely sensed speeds (Davis et al. 2009; Byrne et al. 2010; Howard et al. 2012), and transit-time inferences using a constant speed estimate. The latter is appropriate because this event's speed has been determined to be approximately constant above the corona (Byrne et al. 2010), and we check kinetic energy inferences against the other methods above. Unless specifically noted, all speeds in the following discussion are averages from transit time inferences, from the top of the corona at 0.1 AU to arrival at *ACE*.

The average speed of this CME was slow: 300–430 km s^{-1} across the different portions of the arriving structure. These numbers and geometry are consistent with the timing and stereoscopic analyses performed by Davis et al. (2009) and Byrne et al. (2010). Applying these limits to the mass of 2 Pg at arrival (from Figure 3) gives total kinetic energy limits at arrival of 140 ± 50 ZJ (ZJ = ZettaJoule = 10^{21} J).

Kinetic energy calculation from the CME's evolution is complicated by the fact that the arriving CME contains both original coronal material and swept-up solar wind, which includes a mix of intrinsic kinetic energy from the slow solar wind and that transferred from the rest of the CME. The coronal portion crossed *ACE* over an interval of roughly 36 hr, centered on 2008 December 17. Taking the departure time as 2008 December 12 15:00 UT, when the CME front was near the top of the COR2 field of view (0.1 AU from the Sun), the average transit speed of this centerline is (0.9 AU) $(114\,\mathrm{hr})^{-1}$ or 330 km s^{-1}. Taking the mass of the connected coronal material in the CME to be 1 ± 0.2 Pg (Figure 3), the bulk kinetic energy is thus 55 ± 15 ZJ. Breaking down the components slightly further, we have the front portion of the connected sheath arriving after 104 hr and the back portion after 115 hr. Summing the resultant bulk kinetic energies of the two components yields 60 ± 15 ZJ, which is within the considerable uncertainty of these estimates.

The wind sheath is caught up by the CME in transit, and is composed of the same material, with the same general solar connectivity, as the surrounding wind ahead of the CME. We infer the Δv between the CME and the swept-up material in the wind sheath, using the morphological inferences from the in situ data. From Figure 4, the beginning of the doubly connected sheath, which corresponds to the dredged-up coronal material, traveled 0.9 AU from the top of the COR2 field of view to *ACE* in ∼98 hr, for an average speed of 380 km s^{-1}. We take this front of the coronal sheath to be a piston driving into the solar wind, some of which accretes in front of the piston to form the wind sheath. The front of the wind sheath covered the same 0.9 AU in 89 hr, for an average speed of 420 km s^{-1} and an average growth rate of 40 km s^{-1}. The wind sheath is compressed by a factor of 1.8 compared to the pre-event wind, yielding a Δv of 32 km s^{-1}. This is consistent with the direct proton speed measurements from *ACE*, which show a bulk wind speed close to 330 km s^{-1} before the wind sheath arrival and close to 370 km s^{-1} in the wind sheath. Note that the inferred wind speed (350 km s^{-1}) is thus *faster* than the average speed of the ejected flux rope, although it is slower than the speed of the front of the coronal sheath. Despite uncertainties in the individual speed measurements, this result is strong because it was inferred via a difference rather than by multiple independent measurements. This overexpansion effect has been seen in other events as well (e.g., Gosling et al. 1994, 1998).

Taking the wind sheath mass to be 1 ± 0.2 Pg (from Figure 3), that material's kinetic energy was 60 ± 20 ZJ before interaction with the CME and 90 ± 20 ZJ after it, with the errors between the two estimates correlated (via mass). The CME thus supplied 30 ± 15 ZJ to the wind sheath, a significant fraction of the total kinetic energy on launch. While this number is large, it does not imply the existence of a long-term driver: it is consistent with uncertainty in the initial onset speed of the CME. Taking the initial speed of the CME to be 415 km s^{-1} (the average of the two highest speeds reported by Davis et al. 2009) and the mass to be 1 Pg, the initial kinetic energy was 90 ZJ, enough to account for both the final kinetic energy of the connected sheath and flux rope on arrival (∼60 ZJ) and the additional transferred energy in the wind sheath (∼30 ZJ). Thus this CME was consistent with no additional driving in transit, although some CMEs have been reported to be driven over a significant fraction of 1 AU (e.g., Chen 1996; Manoharan et al. 2001; McIntosh et al. 2007; Howard et al. 2007).

3.4. SECCHI/EUVI and the CME Onset Mechanism

Given the association between the visible corona and the in situ data, it is possible to track the CME back to its origins in the low corona that is visible in the EUV. Morphological analysis of EUV imagery from the *SECCHI*/EUVI instrument connects the pre-eruptive event and its onset mechanism to the features observed in situ by *ACE* and *Wind* some four days later.

Although EUV images are common, the nuances of EUV image interpretation are not familiar to much of the in situ analysis community, and we therefore include a brief overview. Unlike Thomson scattered visible light, coronal EUV emission is largely spectral line emissions from trace ions that are excited collisionally in the low corona, where the mean collision time ranges from a few seconds to a few minutes. For first-order analysis, the coronal abundance fractions are commonly taken to be fixed. Further, the corona is taken to be in local thermal equilibrium between the electron and ion kinetic temperatures and the ionization temperature because of the rapid equilibration time. This leads to a first-order theory in which observed EUV radiance in a particular narrow band of wavelengths (such as seen through a single channel of *STEREO*/EUVI) is the integral along each line of sight of the *squared* electron number density, scaled by a telescope- and spectrum-dependent kernel $K_{\mathrm{tel}}(T)$ that encapsulates the thermal equilibrium, emission physics, and telescope passband. The passband is important because narrow-band EUV telescopes generally admit more than one spectral line, so the function $K_{\mathrm{tel}}(T)$ often contains more than one peak in sensitivity. For example, the EUVI 171 Å band admits two bright spectral lines from Fe IX and Fe X, but also admits a forest of lines from O V, which is present at far cooler temperatures, as well as myriad very faint lines from multiple additional species. Many authors have developed variants of this first-order theory; readers are referred to DeForest et al. (1991) and Brosius et al. (1996) and references therein for details.

The first-order, optically thin theory of EUV emission fails spectacularly in some cases. Although most features in the solar corona are seen as bright in EUV, cool dense structures can be optically thick. Solar prominences can be recognized easily as dark absorption features near the surface of the Sun (e.g., Landi & Reale 2013 and references therein). Although EUV telescope images are commonly called by the peak emission temperature of their dominant spectral lines, or by those lines themselves (e.g., "Fe IX/X" or "1 MK" for the 171 Å images from EUVI), some bright features may be at a different temperature entirely (e.g., DeForest et al. 1991), and in the presence of flow the ionization equilibrium can be very different from the static case (e.g., Esser et al. 1992; Habbal et al. 1993). Nevertheless, because most coronal structures appear to be multithermal (e.g., DeForest 1995; Schmelz et al. 2011 and references therein), and because the plasma β parameter is low in most of the corona, EUV imagery makes a good first-impression diagnostic of both density and magnetic morphology. Features such as cusps and X-points are directly visible morphologically. Other features, such as circular or near-circular cross section voids, hint at magnetic flux rope structures that are not directly visible.

Figure 6 shows the *STEREO-A* view of the CMEs in Figure 2 from EUVI, at four times surrounding the onset of the CMEs;

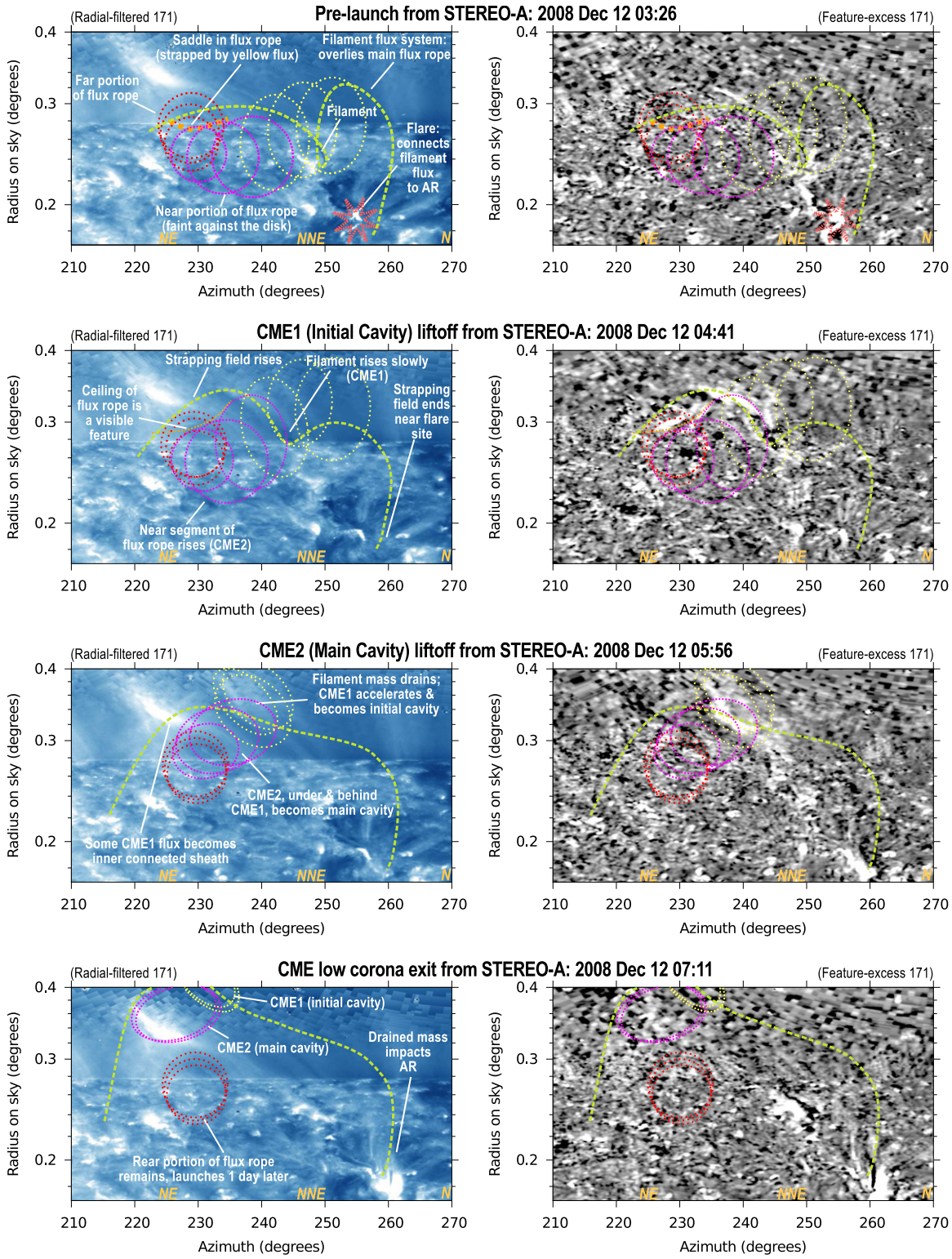

Figure 6. EUVI-A image sequence detailing the launch of the Earth-directed CME of 2008 December 12. Left panels (blue) show direct, radially filtered images; right panels (grey) show excess brightness over the first quartile for each pixel, to highlight evolution of faint features.

(An animation of this figure is available in the online journal.)

Figure 7 shows the same system viewed simultaneously from *STEREO-B*, separated by 90° in longitude (Figure 1). The right-hand column of each figure shows the same images, digitally processed to show excess brightness over the two-hour first-quartile brightness of each pixel. Removing the first-quartile brightness highlights faint brightenings in the resulting images. The two figures support the movie file, available in the online journal, which shows the entire eruption event without overlying markup. We have drawn cartoon imagery of the inferred magnetic structures of interest on the figure panels; the movie has been left with no markup, so that the reader can view the data without distracting overlays.

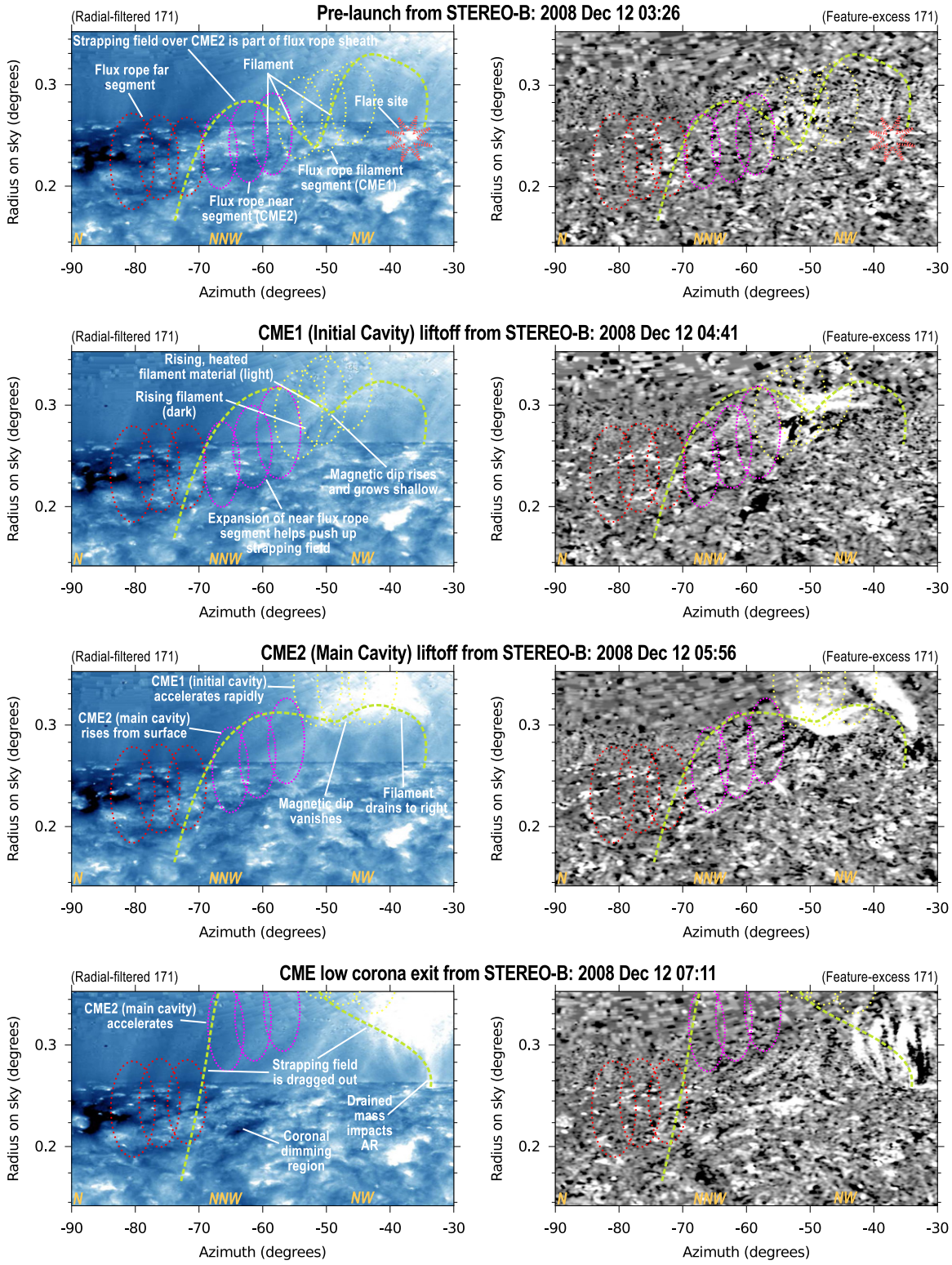

Figure 7. EUVI-B image sequence detailing the launch of the Earth-directed CME of 2008 December 12. Left panels (blue) show direct, radially filtered images; right panels (grey) show excess brightness over the first quartile for each pixel, to highlight evolution of faint features.

(An animation of this figure is available in the online journal.)

In Figures 6 and 7, the left-hand column shows direct EUV exposure data in the 171 Å (Fe IX/X) band, and represents mostly collisionally excited emission from plasma in the 0.9–1.2 MK range. The images have been radially filtered to equalize the mean and standard deviation at each 2-D radius from the Sun center, thereby removing the steep radial gradient in brightness. They have also been transformed to the same projection as Figure 2, so that the radial direction is vertical and the azimuthal direction is horizontal. The two figures have quite different viewpoints (separated by 90° in longitude), and

several corresponding features are marked on the images to help identify major elements of the scene.

Near the top of the EUVI images, large pixelated "chunky" squares are visible; they are also visible at the top of the EUVI portion of Figure 2. This texturing is the result of aggressive image compression on board *STEREO*, together with the faintness of the images near the outer edge of the EUVI field of view. The compression algorithm discards nearly all data from the outer portion of the image, drastically reducing effective resolution, but physically meaningful features can still be seen despite the pixelation.

The cartoon markup in Figures 6 and 7 is based on direct visual identification of features in the corona, using common interpretations. Circular-cross-section cavities in the corona are often seen associated with CMEs (e.g., Gosling et al. 1974) and have been interpreted as partially evacuated flux ropes (e.g., Fuller et al. 2008). Similarly, magnetic dips (as at the bottom of horizontal flux ropes) are known to be locations of coronal condensation that can form prominences (Antiochos & Klimchuk 1991; Antiochos et al. 2000; Karpen et al. 2001; Gibson et al. 2004). Accordingly, we have marked the circular cross-section cavity centered at azimuth 230°, radius 0.̊27 as a possible flux rope (red), and also drawn in a similar flux rope (yellow) over the filament that is visible as a dark absorption feature at azimuth 250°, radius 0.̊24. The intermediate (magenta) section of flux rope/cavity is inferred rather than directly viewed in the *STEREO-A* data, and the reasons why we infer its presence are described in detail below. Although direct magnetic measurements are not available in the low corona, it is possible to draw inferences about magnetic connectivity from the morphology and evolution of the features in the corona. We have drawn a particular inferred field line from the flaring active region at azimuth 257°, radius 0.̊18. The dip portion is inferred from the presence of the filament and the dip model of filament formation (Antiochos & Klimchuk 1991). The connectivity on either side is inferred from activity as the region evolves.

The onset mechanism is far from clear from the *STEREO-A*/EUVI data alone. A small flare at around 03:26 UT, visible at azimuth 255°, radius 0.̊18 from *STEREO-A*, precedes gradual liftoff of the filament at azimuth 255°, radius 0.̊24. The filament liftoff, visible in the movie available in the online journal, clearly coincides with the time and azimuth of appearance of the initial cavity in Figure 2, not the main cavity. It is followed (at about 05:56 UT) by a slight rearrangement of the visible cavity in the streamer belt (at azimuth 230°). After the liftoff, at around 07:11 UT, a rain of bright material falls into the active region at azimuth 260°. There is little sign, at first glance at the EUV images, of what feature becomes the main cavity.

Flux ropes that are not exactly aligned with the viewing angle are difficult or impossible to distinguish against the bright background of the corona because they are nearly evacuated and hence do not emit much EUV, so it is necessary to refer to secondary clues in the image sequence. The liftoff of the filament and its presumed associated flux rope coincides in ejection angle and timing with the leading cavity, not the main cavity, indicating that it is not the origin of the main Earth-directed CME. The single visible round cavity at left in the *STEREO-A* view (marked "Far portion of flux rope" in the top panel of Figure 6) does not erupt with the initial CMEs. We infer the presence of a third segment of flux rope (marked "Near portion of flux rope" in the top panel of Figure 6), that erupts to become the primary CME cavity and flux rope, from two subtle but unmistakable cues.

First, during the liftoff of the filament, the "haze" at the top of the stationary cavity shifts, forming a small bright feature that we interpret to be a visual caustic[4] that is formed by distortion of a flux rope ceiling. This feature is marked in the top row as "Saddle in flux rope" and in the second panel with "Ceiling of flux rope." The brightness feature is clearly visible in the right-hand column, second row, at azimuth 230°, radius 0.̊30. Using this frame as a guide, it is possible to observe the formation, motion, and subsequent fading of this caustic in the accompanying movie.

Secondly, the view from *STEREO-B* shows a single linear dimming region that forms after the liftoff of the CMEs. The dimming region extends along the "floor" of the corona from the location of the pre-eruption prominence to the location of the static flux rope segment. We interpret the dimming region to be the footprints of newly stretched field lines that are entrained in the eruption (e.g., Webb et al. 2000), and infer from the extent of the dimming region in the *STEREO-B* imagery that a single flux rope extends from the static cavity across the *STEREO-B* field of view to the space above the prominence. This is drawn in all the images as the magenta flux rope segment (the middle of three) in both Figures 6 and 7. The segment connecting the far flux rope and the prominence flux rope is foreshortened, but not fully end-on, in the *STEREO-A* images. This makes visual detection difficult against the clearer background structure of the far flux rope segment.

From the *STEREO-B* vantage in Figure 7, several other important aspects of the liftoff become clear. In particular, the flux system that gives rise to the CMEs is presented more cleanly: the lines of sight pass across, rather than nearly along, the main axis of the flux rope. The flare site is visible at the upper right, and several other corresponding features are readily identified. In the *STEREO-B* sequence, we see that the flare and rising filament are accompanied by a rise in the top of the central portion of the flux rope (note the bright sloping and horizontal caustics, particularly in the right column, in the 04:41 UT exposure at azimuth −65° and radius 0.̊28), matching the evolution of the caustic seen in the same panel in Figure 6.

The frames at 04:41 UT and 05:56 UT explain the "rain" seen by *STEREO-A* at 07:11 UT: it is prominence and compressed coronal material, heated and lifted over the top of the flux rope as the magnetic dip associated with the prominence disappears. We surmise that the brightness of the material in the field of view is due to the forest of O v lines present in the 171 Å band at about $10^{5.4}$ K, rather than the main Fe ix and x lines present at about $10^{6.0}$ K; thus, the prominence material has likely not undergone strong heating. The material's motion, heating (transition from EUV-dark to EUV-bright), and draining are clearly visible from the *STEREO-B* vantage. The material drains down the still-connected southern flank of the flux rope to impact at or very near to the initial flare site. The high altitude material is not visible in Figure 6 because from that perspective it is seen against the far brighter disk in the background. In Figure 7, the material is above the limb in the plane of the sky, so that it is visible against the darker background relatively high in the corona.

[4] Readers are reminded that a caustic in a mapping between two coordinate systems is a locus where the determinant of the Jacobian of the mapping is zero. If the mapping is from an optically thin, bright 2-D curved manifold to an image plane, then these loci form especially bright features on the image plane. The caustic in the second row of Figure 6 results from a transient alignment between the cavity ceiling and the line of sight.

While the flux rope and its changes are only faintly visible in Figure 7, its extent is readily identified via the dark coronal dimming region that begins at 07:11 UT near −65° azimuth, and extends down and left. In images subsequent to 07:11 UT (and in the accompanying digital movie), it is possible to trace the flux rope's entire length by the extended coronal dimming region left behind after the ultimate eruption of the third segment of the flux rope a day after the main eruption.

From the EUVI morphological analysis, a clear narrative emerges. A flux rope structure forms in the corona some time before the onset events on 2008 December 12. The flux rope forms a prominence in dips near the active region at 255° azimuth in Figure 6. A small flare (starburst in the top panels of Figures 6 and 7) connects the flux rope directly to one side of the active region, and destabilizes the near portion of the flux rope (sketched in yellow in Figures 6 and 7). The outermost field lines of the flux rope (one is drawn) thread through the filament and over the central portion (sketched in magenta), serving as a strapping field to retain the central portion of the flux rope. As the filament lifts off, these field lines destabilize the magenta portion of the flux rope, and the system gradually lifts off the surface of the Sun. When the strapping field lines rise high enough, the filament material drains, giving rise to a mass-draining instability. The yellow portion of the flux rope accelerates rapidly, together with one end of the strapping field lines from the magenta portion. This allows the magenta portion, too, to erupt.

The yellow portion of the flux rope becomes the "initial cavity" seen in Figure 2, and the magenta portion of the flux rope becomes the "main cavity" and the magnetic cloud that impact *ACE* and *Wind*. The proximal cause of the main cavity eruption is the mass-draining instability, confirming the interpretation of the in situ data—although the mass-draining itself was triggered by the slow liftoff of the prominence, which was enabled by tether cutting in the small flare at 03:26 UT.

The static (red-marked) portion of the flux rope remains intact through the initial CME liftoff; it appears to be held down by strapping field that also forms the visible streamer even in the bottom panels of Figure 6. In subsequent images on 2008 December 13, that portion also erupts in a kink-and-rise scenario similar to those described by Fan & Gibson (2003) and Rachmeler et al. (2009).

Thus, although the 2008 December 12 CME proper was released through mass draining, it is associated with three major onset instabilities that applied to different portions of the same long flux rope on the solar surface: tether cutting reconnection, mass draining, and the kink instability.

4. CONCLUSIONS

By combining qualitative EUV imagery, quantitative visible imagery, and in situ observations, we have arrived at a complete picture of the onset and behavior of a slow, flux-rope-containing CME that did not give rise to a shock in the solar wind. In particular, we have found that the in situ and imaging data are consistent with the presence of pre-existing "strapping field" and other coronal structures, essentially intact, in the sheath region around the front of the CME near 1 AU. This view is corroborated by morphological analysis of simultaneous EUVI imagery from *STEREO-A* and *STEREO-B* during the liftoff phase of the CME. These intact structures from the low corona are preserved beneath/behind a layer of accumulated solar wind material that is compressed onto the front of the erupting closed magnetic structures as they propagate through the corona and heliosphere.

Our identification of the major anatomical elements of the CME is enabled by combining morphological analysis of the pre-eruption structure and the sequence of events during onset from two viewpoints; continuous remote tracking via Thomson scattered light; remote quantitative mass measurements via photometry; and the three key in situ parameters of solar wind density, magnetic field, and suprathermal electron pitch angle distribution.

The ability to diagnose and trace the coronal strapping field, in particular, is a new indicator of the CME onset mechanism. The "breakout" model, for example, requires that the strapping field over the CME open as part of the launch process (Antiochos et al. 1999; Lynch et al. 2008). By tracing individual components of the CME from Sun to Earth, we determined that the 2008 December CME was launched by some instability other than breakout, such as mass draining. This conclusion was corroborated by morphological analysis of EUVI imagery.

EUVI morphological analysis from two separate viewpoints revealed both the complexity of the onset process for this CME and the difficulty of determining the presence or absence of a flux rope from morphological cues alone: the *STEREO-B* data, for example, show no clearly defined structure where we know (from the *STEREO-A* images) the flux rope to be. This is because at viewing angles far from the axis of the flux rope, there is little or no EUV contrast to show the structure. Likewise, some events (such as the mass draining event that destabilizes the initial portion of the flux rope) are visible with *STEREO-B* but invisible in the *STEREO-A* data, due to coincidences of alignment. Both spacecraft were required to piece together the puzzle posed by the EUVI image sequence.

Our conclusion that this CME was not launched by breakout is not, in itself, remarkable: breakout is primarily used to explain fast CMEs, and this CME launched slowly. But it shows that quantitative remote sensing and in situ monitoring can be combined to diagnose onset mechanism in other, more energetic CMEs by tracking the coronal remnants from the Sun to in situ probes directly, and by examining the accumulation of mass as the feature transits the solar system.

In contrast, the complicated nature of the release of the entire flux rope is remarkable. At least three of the major release mechanisms played a role in liftoff of this long flux rope (tether cutting reconnection, mass draining, and the kink instability). That reflects the complex magnetic connectivity of the lower corona and demonstrates the importance of unified analysis from multiple instruments to understand the complex processes involved in destabilizing and launching even "garden variety" CMEs.

The ability to track features continuously forward and backward in time via heliospheric imaging has enabled, for the first time, identification of particular pieces of the low corona that later impact Earth. For example, we have established that the bright feature identified in the second row of Figure 6 as "Ceiling of flux rope" forms the inner part of the "coronal sheath" observed in situ at *ACE* and shown in Figure 4.

Quantitative Thomson-scattered imaging enables measurement of the mass of the event regardless of shape. This allows positive identification of the different portions of the CME anatomy, as seen in in situ data, based on their growth enroute. It also enables direct calculation of extrinsic quantities such as total mass or kinetic energy of the system, which are otherwise

not accessible without modeling. By contrast, in situ measurements can only measure intrinsic quantities, such as density or kinetic energy density per particle, that are available locally rather than integrated over the whole structure. Combining remote and in situ measurements should, in turn, enable resolution of longstanding questions such as the energy balance of CMEs enroute and whether some CMEs have a long-term driver; how the detailed, currently unresolved structure of CMEs evolves to become the fine-scale features observed in situ; and how coronal morphology and resultant CME onset affects CME energy and geoeffectiveness.

The authors acknowledge and thank J. Gosling for his extensive help, particularly with interpreting the in situ data, and also the *STEREO*, *ACE*, and *Wind* instrument teams for making their data available. Additionally, the work benefited from insightful conversations and data retrieval help from H. Elliott, R. Skoug, K. Ogilvie, A. Reinard, and J. Tappin; and also from insightful comments by the anonymous referee. Our image processing made heavy use of the freeware Perl Data Language (http://pdl.perl.org). This work was supported by NASA's SHP-GI program (grant NNG05GK14G) and SHP-SR&T program (grant NNX13AF98G), and by the NSF SHINE Competition (grant ATM-0849916).

REFERENCES

Aly, J. J. 1984, ApJ, 283, 349
Aly, J. J. 1991, ApJL, 375, L61
Antiochos, S. K., DeVore, C. R., & Klimchuk, J. A. 1999, ApJ, 510, 485
Antiochos, S. K., & Klimchuk, J. A. 1991, ApJ, 378, 372
Antiochos, S. K., MacNeice, P. J., & Spicer, D. S. 2000, ApJ, 536, 494
Brosius, J. W., Davila, J. M., Thomas, R. J., & Monsignori-Fossi, B. C. 1996, ApJS, 106, 143
Brueckner, G. E., Howard, R. A., Koomen, M. J., et al. 1995, SoPh, 162, 357
Burlaga, L. F. 1988, JGR, 93, 7217
Burlaga, L. F., Sittler, E., Mariani, F., & Schwenn, R. 1981, JGR, 86, 6673
Byrne, J. P., Maloney, S. A., McAteer, R. T. J., Refojo, J. M., & Gallagher, P. T. 2010, NatCo, 1, 74
Cane, H. V., & Richardson, I. G. 2003, JGRA, 108, 1156
Chen, J. 1989, ApJ, 338, 453
Chen, J. 1996, JGR, 101, 27499
Davis, C. J., Davies, J. A., Lockwood, M., Rouillard, A. P., & Eyles, C. J. 2009, GeoRL, 36, L08102
DeForest, C. E. 1995, PhD thesis, Stanford University
DeForest, C. E., Howard, T. A., & McComas, D. J. 2012, ApJ, 745, 36
DeForest, C. E., Howard, T. A., & Tappin, S. J. 2011, ApJ, 738, 103
DeForest, C. E., Kankelborg, C. C., Allen, M. J., et al. 1991, OptEn, 30, 1125
Dryer, M., Wu, S. T., Wu, C. C., & Han, S. M. 1992, in Proc. 26th ESLAB Symposium on Study of the Solar-Terrestrial System (ESA SP-346; Noordwijk: ESA), 77
Esser, R., Habbal, S. R., & Arndt, M. B. 1992, in Proceedings of the First SOHO Workshop: Coronal Streamers, Coronal Loops, and Coronal and Solar Wind Composition (ESA SP-348; Noordwijk: ESA), 277
Fan, Y., & Gibson, S. E. 2003, ApJL, 589, L105
Fan, Y., & Gibson, S. E. 2004, ApJ, 609, 1123
Fan, Y., & Gibson, S. E. 2007, ApJ, 668, 1232
Fong, B., Low, B. C., & Fan, Y. 2002, ApJ, 571, 987
Forbes, T. G. 2000, JGR, 105, 23153
Fuller, J., Gibson, S. E., de Toma, G., & Fan, Y. 2008, ApJ, 678, 515
Gibson, S. E., & Fan, Y. 2006, JGRA, 111, 12103
Gibson, S. E., Fan, Y., Mandrini, C., Fisher, G., & Demoulin, P. 2004, ApJ, 617, 600
Gopalswamy, N., Yashiro, S., Michalek, G., et al. 2009, EM&P, 104, 295
Gosling, J. T. 1990, GMS, 58, 343
Gosling, J. T. 1993, JGR, 981, 18937
Gosling, J. T., Baker, D. N., Bame, S. J., et al. 1987, JGR, 92, 8519
Gosling, J. T., Bame, S. J., McComas, D. J., et al. 1994, GeoRL, 21, 237
Gosling, J. T., Birn, J., & Hesse, M. 1995, GeoRL, 22, 869
Gosling, J. T., Hildner, E., MacQueen, R. M., et al. 1974, JGR, 79, 4581
Gosling, J. T., McComas, D. J., Phillips, J. L., & Bame, S. J. 1992, JGR, 97, 6531
Gosling, J. T., Riley, P., McComas, D. J., & Pizzo, V. J. 1998, JGR, 103, 1941
Habbal, S. R., Esser, R., & Arndt, M. B. 1993, ApJ, 413, 435
Howard, R. A., Sheeley, N. R., Michels, D. J., & Koomen, M. J. 1985, JGR, 90, 8173
Howard, T. A., & DeForest, C. E. 2012a, ApJ, 746, 64
Howard, T. A., & DeForest, C. E. 2012b, ApJ, 752, 130
Howard, T. A., DeForest, C. E., & Reinard, A. A. 2012, ApJ, 754, 102
Howard, T. A., Fry, C. D., Johnson, J. C., & Webb, D. F. 2007, ApJ, 667, 610
Hudson, H. S., Bougeret, J.-L., & Burkepile, J. 2006, SSRv, 123, 13
Hundausen, A. J. 1993, JGR, 98, 13177
Illing, R. M. E., & Hundhausen, A. J. 1986, JGR, 91, 10951
Karpen, J. T., Antiochos, S. K., Hohensee, M., Klimchuk, J. A., & MacNeice, P. J. 2001, ApJ, 553, 85
Klein, L. W., & Burlaga, L. F. 1982, JGR, 87, 613
Klimchuk, J. A., & Sturrock, P. A. 1992, ApJ, 385, 344
Landi, E., & Reale, F. 2013, ApJ, submitted
Lepping, R. P., Acũna, M. H., & Burlaga, L. F. 1995, SSRv, 71, 207
Liu, Y., Davies, J. A., Luhmann, J. G., et al. 2010, ApJL, 710, L82
Low, B. C. 1996, SoPh, 167, 217
Lugaz, N. 2010, SoPh, 267, 411
Lugaz, N., Farrugia, C. J., Davies, J. A., et al. 2012, ApJ, 759, 68
Lynch, B. J., Antiochus, S. K., DeVore, C. R., Luhmann, J. G., & Zurbuchen, T. H. 2008, ApJ, 683, 1192
MacQueen, R. M., Csoeke-Poeckh, A., Hidlner, E., et al. 1980, SoPh, 65, 91
Manoharan, P. K., Tokmumaru, M., Pick, P., Subramanian, P., et al. 2001, ApJ, 599, 1180
McComas, D. M., Bame, S. J., Barker, P., et al. 1998, SSRv, 86, 563
McIntosh, S. W., Leamon, R. J., Davey, A. R., & Wills-Davey, M. J. 2007, ApJ, 660, 1663
Moore, R. L., Hagyard, M. J., & Davis, J. M. 1987, SoPh, 113, 347
Moore, R. L., & Roumeliotis, G. 1992, in Eruptive Solar Flares, ed. Z. Svestka, B. V. Jackson, & M. E. Machado (New York: Springer), 69
Möstl, C., Farrugia, C. J., Kilpua, E. K. J., et al. 2012, ApJ, 758, 10
Ogilvie, K., Chornay, D. J., & Fritzenreiter, R. J. 1995, SSRv, 71, 55
Rachmeler, L. A., DeForest, C. E., & Kankelborg, C. C. 2009, ApJ, 693, 1431
Savani, N. P., Shiota, D., Kusano, K., Vourlidas, A., & Lugaz, N. 2012, ApJ, 759, 103
Schmelz, J. T., Jenkins, B. S., Worley, B. T., et al. 2011, ApJ, 731, 49
Smith, C. W., L'Heureux, J., Ness, N. F., et al. 1998, SSRv, 86, 613
Sturrock, P. A. 1991, ApJ, 380, 655
Török, T., & Kliem, B. 2003, A&A, 406, 1043
Török, T., & Kleim, B. 2005, ApJL, 630, L97
Webb, D. F., Lepping, R. P., Burlaga, L. F., et al. 2000, JGR, 105, 27251
Wood, B. E., Rouillard, A. P., Möstl, C., et al. 2012, SoPh, 281, 369
Zhou, G. P., Wang, J. X., Zhang, J., et al. 2006, ApJ, 651, 1238
Zurbuchen, T. H., & Richardson, I. G. 2006, SSRv, 123, 31